

Some Numerical Issues on Simulation of Detonation Cell Structures

J. Y. Choi,¹ F. H. Ma,² and V. Yang²

UDC 536.46

Translated from *Fizika Goreniya i Vzryva*, Vol. 44, No. 5, pp. 72–92, September–October, 2008.
Original article submitted July 3, 2007.

The present study examines several numerical issues on simulation of detonation cell structures. Various stability regimes ranging from weakly to highly unstable detonations are considered. The analysis treats two-dimensional inviscid fluid-dynamics equations and a one-step reaction model. A series of investigations is carried out to identify numerical requirements for high-fidelity simulations of detonation cell structures. Emphasis is placed on the wave-front dynamics and evolution of cellular patterns. The effects of the preexponential factor, grid size, time step, domain length, and exit boundary condition on the cellular structure and cell size are examined systematically. The required numerical grid size is determined and compared with various length scales associated with a steady Zel'dovich–von Neumann–Döring detonation wave. A general rule for the grid-resolution requirement is proposed for the first time: a minimum of 5 grid points should be included in the heat-release zone of the corresponding steady Zel'dovich–von Neumann–Döring detonation wave, in order to achieve an accurate simulation of detonation cell structures.

Key words: shock wave, detonation cells, numerical simulation.

INTRODUCTION

It is well established that a gaseous detonation wave typically has a cellular structure that involves triple-shock interactions [1]. In experiments, as the detonation wave propagates, the traces of this structure are revealed as the so-called detonation cells on a wall coated with a thin layer of soot or smoke foil. This paper attempts to identify the computational requirements for accurately predicting the cellular structures of two-dimensional detonation waves in various stability regimes.

Extensive numerical simulations have been conducted [2–13] to investigate gaseous detonation-wave structures. Table 1 summarizes the reactants, chemical kinetics model, computational domain, grid resolution, initial perturbation, and calculated detonation cell size in each of those studies. Earlier work was based on relatively simple approaches, mainly due to limitations

in computer resources. Oran et al. [2] demonstrated the growth of transverse perturbations from an initially inclined shock using a one-step induction-parameter model. Taki and Fujiwara [3] explored the triple-shock behavior of H₂–O₂–Ar detonation in a narrow channel. The final number of transverse shock waves was found to be insensitive to the number of initial exothermicity spots used to perturb a Chapman–Jouguet (CJ) detonation wave. Kailasanath et al. [4] estimated the detonation cell size of an H₂–O₂–Ar mixture by systematically varying the channel width. The spatial resolutions in these early studies ranged between 40 and 80 grid points per cell width.

With recent advances in computing power, much finer grid resolutions and more complete chemical kinetics schemes have been adopted. Using a grid resolution of about 20 grid points per half-reaction length, Bourlioux and Majda [5] resolved detonation cells in narrow channels for various heat releases and activation energies. Encouraging agreement was achieved between computed cell widths and predictions from detonation instability theories. Oran et al. [6] simulated detona-

¹Pusan National University, Busan 609-735, Korea.

²The Pennsylvania State University,
University Park, PA 16802, USA; vigor@psu.edu.

TABLE 1

Survey of Numerical Studies on the Cellular Structure of Gaseous Detonation Waves

Reference, year	Reactants	Kinetics	Domain size	Grid size	Simulated cell width	Initial perturbation
Oran et al. [2], 1981	H ₂ /air 1 atm; 300 K	1-step induction	82.5 × 0.45 cm	0.15 mm	0.9 cm	Inclined initial shock
Taki et al. [3], 1981	H ₂ /O ₂ /Ar 1 atm	2-step induction	100L _{ind} × 20L _{ind} (L _{ind} ≈ 2.25 mm)	L _{ind} /4	≈10L _{ind}	Hot spot in unburned mixture
Kailasanath et al. [4], 1985	H ₂ /O ₂ /Ar 8.66 kPa; 298 K	1-step induction	W = 5–10 cm	0.1–0.2 cm	≈8.5 cm	Elliptical unreacted pocket
Bourlioux et al. [5], 1992	—	1-step Arrhenius	W = 5.7L _{1/2} (Case A)	L _{1/2} /17	5.7L _{1/2}	Linear unstable traveling or standing modes
Oran et al. [6], 1998	H ₂ /O ₂ /Ar 6.67 kPa; 298 K	48 steps 8 species	W = 6 cm	Δx = 0.15 mm Δy = 0.235 mm (benchmark)	3 cm	Rectangular unreacted pocket
Gamezo et al. [7], 1999	H ₂ /O ₂ 1 atm; 293 K	1-step Arrhenius	W = 0.3 cm	0.01 mm	≈0.08 cm	None
Singh et al. [8], 1999	—	—//—	W = 10L _{1/2} (L _{ind} ≈ 5.4 mm)	L _{1/2} /24–L _{1/2} /2	≈10L _{1/2}	Sinusoidal perturbation
Nikolic et al. [9], 1999	—	—//—	W = (0.5–100)L _{1/2}	L _{1/2} /40–L _{1/2} /20	(5–15)L _{1/2}	Sinusoidal density perturbation at shock
Gavrikov et al. [10], 2000	—	—//—	—	100 grid points per cell width	—	None
Sharpe et al. [11], 2001	—	—//—	≈400L _{1/2} × 10L _{1/2}	L _{1/2} /64–L _{1/2} /4	≈10L _{1/2}	Density perturbation in front of shock
Hu et al. [12], 2004	H ₂ /O ₂ /Ar 6.67 kPa; 298 K	19-step 9-species	W = 2 cm	0.025–0.2 mm (L _{ind} ≈ 1.6 mm)	0.8 cm	Random perturbed specific energy
Liang et al. [13], 2005	—	4-step	50L _{1/2} × ×(2.5–10)L _{1/2}	L _{1/2} /64	≈10L _{1/2}	Sinusoidal disturbance in velocity
Present work	—	1-step Arrhenius	W = 1 (in rel. units)	L _{h.r.} /5	—	Inclined detonation wave

Note. L_{ind} is the length of the induction zone, L_{1/2} is the length of the half-reaction zone, and L_{h.r.} is the length of the heat-release zone.

tion waves in a low-pressure $\text{H}_2\text{-O}_2\text{-Ar}$ mixture using a detailed chemical reaction mechanism. Much information about the cellular structure was obtained, including the formation of unreacted pockets, collision of triple points, and evolution of the transverse waves. A grid-sensitivity study was also conducted by varying the spatial resolution in the range of 100 to 800 grid points per cell width (equal to half of the channel width). It was found that all grids gave an almost equal cell size, except that the coarsest grid led to two more weak triple points. A spatial resolution with 130 grid points per cell width (the second coarsest grid) could thus be considered to provide sufficient resolution of detonation cells for the cases in the study. Gamezo and Desbordes [7] examined the effect of activation energy on the regularity of the cellular structure. In their simulations, numerical noise and machine errors seemed strong enough to excite the formation of transverse waves. Each cell width contained 80 grid points. Singh et al. [8] conducted simulations for both inviscid and viscous flows, with grid sizes varying from $L_{1/2}/24$ to $L_{1/2}/2$ ($L_{1/2}$ is the length of the half-reaction zone). With coarse grids, the numerical dissipation overshadows its physical counterpart, leading to similar solutions for inviscid and viscous flows. The situation is different, however, for fine grids. Numerical dissipation and grid resolution thus play a significant role in determining cellular structures for inviscid flows. Nikolic et al. [9] studied the effect of the channel width, in the range of $(0.5\text{--}100)L_{1/2}$, on the detonation cell size. No cell was observed for channels with the width smaller than $2.95L_{1/2}$. A half cell and then a full cell appear as the channel width increases to $5L_{1/2}$. The cell width reaches a constant value of about $13L_{1/2}$ for channel widths greater than $40L_{1/2}$.

The issue of grid resolution in simulations of detonation cell structures was further studied recently. Gavrikov et al. [10] correlated calculated detonation cell sizes with characteristic reaction zone lengths and reported that more than 30 grid points for each detonation cell width are required to provide proper resolution of cell structures. Sharpe [11] examined the influence of grid resolution on the detailed structure within a detonation cell. It was suggested that a minimum of 20 grid points in the half-reaction length of the underlying steady detonation wave be used to resolve wave front structures. Hu et al. [12] simulated the cellular structure and its evolution in a low-pressure $\text{H}_2\text{-O}_2\text{-Ar}$ mixture using a 19-step, 9-species reaction model. The grid resolution varied from 8 to 64 grid points per induction zone length. The calculated structure displays different levels of detail with different grid sizes, whereas the detonation cell sizes remain nearly unchanged. Liang and Bauwens [13], using a grid resolution with up to 128

grid points per half-reaction length, studied the detonation wave structure with a four-step chain-branching reaction model. The keystone features behind the shock front, as reported in experiments [14], were observed in the reactant mass-fraction field.

In spite of the substantial progress achieved so far in advancing the understanding of detonation cellular structures, there are still some open questions concerning the numerical requirements for high-fidelity simulations. As can be seen from Table 1 and as discussed above, several different length scales, including the cell width and the induction-zone and half-reaction lengths, have been employed to characterize the grid resolution. No general rule on grid resolution has been proposed for resolving detonation cell structures. The selection of a proper computational domain and the effect of numerical dissipation have not yet been clearly determined. The present study attempts to clarify those issues. Emphasis is placed on the effects of grid resolution, computational domain, and boundary conditions (BC) on calculated detonation cell structures. A general rule on grid-resolution requirements will be established to provide a useful guideline for future studies of detonation cell structures.

1. THEORETICAL AND NUMERICAL FRAMEWORK

1.1. Governing Equations

To focus on numerical issues, a simple yet realistic formulation is employed. The analysis is based on the two-dimensional conservation equations for an inviscid, chemically reacting flow. The reaction rate is expressed with a single progress variable. All the flow variables are normalized by the reference pressure (p^*), temperature (T^*), density (ρ^*), and velocity ($u^* \equiv \sqrt{p^*/\rho^*}$). The reference length and time scales are L^* and $t^* \equiv L^*/u^*$, respectively. The set of conservation equations can be expressed in the nondimensional form [15]

$$\frac{\partial}{\partial t} \begin{bmatrix} \rho \\ \rho u \\ \rho v \\ \rho e \\ \rho Z \end{bmatrix} + \frac{\partial}{\partial x} \begin{bmatrix} \rho u \\ \rho u^2 + p \\ \rho uv \\ u(\rho e + p) \\ \rho uZ \end{bmatrix} + \frac{\partial}{\partial y} \begin{bmatrix} \rho v \\ \rho uv \\ \rho v^2 + p \\ v(\rho e + p) \\ \rho vZ \end{bmatrix} = \begin{bmatrix} 0 \\ 0 \\ 0 \\ 0 \\ \dot{\omega} \end{bmatrix}, \quad (1)$$

where ρ is the density, u and v are the velocity components, and e is the specific total energy. The reaction progress variable Z accounts for the mass fraction of product species. The chemical kinetics is modeled by a one-step Arrhenius-type reaction

$$\dot{\omega} = \rho(1 - Z)K \exp(-T_a/T), \quad (2)$$

where $\dot{\omega}$ is the mass rate of product formation, T_a is the activation temperature, and K the preexponential factor normalized by $K^* \equiv 1/t^*$. The pressure p and temperature T are obtained through the equations of state

$$p = (\gamma - 1)\rho\{e - (u^2 + v^2)/2 + Zq\}, \quad (3)$$

$$T = p/(\rho R), \quad (4)$$

where q is the heat release per unit mass of product species. The gas constant R normalized by $R^* \equiv p^*/(\rho^*T^*)$ and the specific heat ratio γ of the mixture are calculated as

$$R = R_1(1 - Z) + R_2Z, \quad (5)$$

$$\gamma = \frac{(1 - Z)R_1\gamma_1/(\gamma_1 - 1) + ZR_2\gamma_2/(\gamma_2 - 1)}{(1 - Z)R_1/(\gamma_1 - 1) + ZR_2/(\gamma_2 - 1)}, \quad (6)$$

where the subscripts 1 and 2 represent unburned (reactant) and burned (product) gases, respectively.

A total of seven model parameters are involved in the formulation: the specific heat ratios (γ_1 and γ_2) and gas constants of reactants and products (R_1 and R_2), the heat release q , the preexponential factor K , and the activation temperature T_a . Their specific values will be discussed later.

1.2. Numerical Method

The governing equations are numerically solved using a cell-vertex finite-volume method. The convective fluxes are calculated by Roe's approximate Riemann solver, with the primitive variables interpolated by a third-order accurate MUSCL-type total variation diminishing (TVD) scheme. The discretized equations are integrated in time using a fourth-order accurate Runge-Kutta scheme. Details of the implementation and accuracy of the numerical scheme were discussed in depth in [16, 17].

1.3. Scaling Issue

A rigorous assessment of grid-resolution requirements is a crucial issue in the present study. The work is very laborious, especially for problems covering a wide range of flow conditions. To facilitate the analysis, the

issue of grid resolution can be addressed by varying the value of the nondimensional preexponential factor K with a fixed grid, as follows.

The dimensionless conservation equation of the reaction progress variable Z is expressed as

$$\begin{aligned} & \frac{\partial \rho Z}{\partial t} + \frac{\partial \rho u Z}{\partial x} + \frac{\partial \rho v Z}{\partial y} \\ & = \rho(1 - Z)K \exp\left(-\frac{T_a}{T}\right), \end{aligned} \quad (7)$$

where the preexponential factor K is related to its dimensional counterpart \tilde{K} through the time scale L^*/u^* :

$$K = \tilde{K}/K^* = \tilde{K}L^*/u^*. \quad (8)$$

If the dimensional preexponential factor \tilde{K} and velocity scale u^* are fixed, K is proportional to the physical length scale considered. Thus, for a given dimensionless grid size, a high value of K corresponds to a large length scale and, consequently, a coarse grid resolution within the reaction zone, whereas a low value of K represents a fine grid resolution. Hence, a grid resolution study for cases with a fixed dimensional preexponential factor \tilde{K} is equivalent to a study of the effect of the dimensionless preexponential factor K with a fixed grid.

2. SIMULATION CONDITIONS

2.1. Model Problem and Boundary and Initial Conditions

The model problem of concern involves detonation wave propagation from the right to the left end of a two-dimensional channel. To avoid the use of a large computational domain to capture this process, a reference frame designed to resolve the detonation wave front is implemented, as shown schematically in Fig. 1. At the left boundary (inlet), fresh reactants enter the computational domain at a supersonic speed. The pressure and temperature are prespecified, and the axial velocity is chosen to be the Chapman-Jouguet detonation speed.

At the right boundary (exit), the CJ condition (i.e., a unity Mach number) can be enforced for a sufficiently long computational domain. In practice, a relatively short domain is used to save computational cost, and an appropriate exit boundary condition should be specified. Gamezo and Desbordes [7] introduced a relaxation method by evaluating the flow properties at the exit boundary as a weighted average of the value at the first grid point next to the boundary and a prespecified farfield property. In the present work, three different types of exit boundary conditions are considered and

TABLE 2

Summary of Numerical Grids		
Grid system	Minimum spacing	Domain size
301 × 101 (uniform 201 × 101 and stretching 2% 100 × 101)	$\Delta x_{\min} = \Delta y = 0.01$	5.18 × 1.0
501 × 201 (uniform 401 × 201 and stretching 3% 100 × 201)	$\Delta x_{\min} = \Delta y = 0.005$	5.13 × 1.0
901 × 401 (uniform 801 × 401 + and stretching 3% 100 × 401)	$\Delta x_{\min} = \Delta y = 0.0025$	5.22 × 2.0

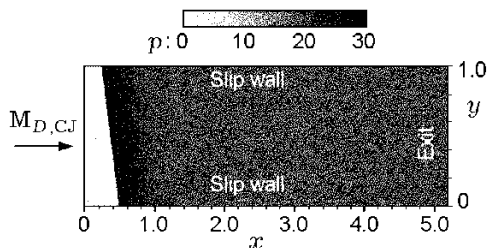


Fig. 1. Computational grid overlaid by the initial pressure distribution.

compared. The first type is a simple extrapolation of flow variables from the interior points. The second type imposes a forced condition to meet the CJ state: extrapolation from the interior points when the flow speed is supersonic, or enforcement of a sonic condition along with a CJ pressure and temperature when the flow is subsonic. The third type is based on the characteristic boundary condition using the CJ state as a farfield condition

$$p_{\text{exit}} = p_{\text{CJ}}, \quad (9)$$

$$\rho_{\text{exit}} = \rho_{\text{exit}-1} + (p_{\text{exit}} - p_{\text{exit}-1})/a_{\text{CJ}}^2, \quad (10)$$

$$u_{\text{exit}} = u_{\text{exit}-1} + (p_{\text{exit}} - p_{\text{exit}-1})/(\rho a)_{\text{CJ}}, \quad (11)$$

where the subscript $\text{exit} - 1$ stands for the value at the first grid point next to the exit boundary and a is the velocity of sound. The transverse velocity component v is simply extrapolated. The third type boundary condition is used for most cases in this paper. Both walls are assumed to be slip and adiabatic.

The one-dimensional Zel'dovich-von Neumann-Döring (ZND) wave structure is employed as the initial condition for two-dimensional simulations. The wave is inclined in the transverse direction to provide flow disturbances for triggering instabilities, as shown in Fig. 1. The reference pressure p^* , temperature T^* , and density ρ^* are taken to be the corresponding flow properties of the fresh reactants, the reference velocity is

$u^* \equiv \sqrt{p^*/\rho^*}$, and the reference length L^* is chosen as the dimensional channel width.

2.2. Numerical Smoke Foil

The shear stress around the triple point in the detonation wave front is known as the physical mechanism of smoke-foil inscription, which can be numerically reproduced based on the peak pressure in the flowfield [13]. In the present paper, the smoke-foil record is obtained by registering the peak pressure behind the shock wave across the width of the computational domain and performing the following transformation from the wave-attached computational coordinate to the laboratory coordinate:

$$x = x_{\text{shock}} - u_1 t. \quad (12)$$

2.3. Computational Grids

A two-dimensional channel with a width of unity is considered. The computational domain contains a dense grid with high resolution to capture the detonation wave front and reacting flow process in the upstream region ($0 \leq x \leq 2$) and a stretched grid in the downstream region ($x \geq 2$). The grid size in the former region is uniform in both the axial and transverse directions, in order to properly describe the transverse shock waves, which are an essential part of the triple-point structure that inscribes cells on smoked foil. The grid is stretched axially in the downstream region to reduce computational costs. The length of the computational domain is appropriately chosen such that the CJ state either resides in the domain or is approximately attained at the exit boundary. The effect of grid resolution is assessed by varying the preexponential factor K . In addition, three different grids, as summarized in Table 2, are employed to further verify the results.

TABLE 3

Summary of Numerical Cases

θ	Cases	Half-reaction and heat-release zone lengths
5.2	Weakly unstable detonation ($2\text{H}_2 + \text{O}_2 + 12\text{Ar}$, $\gamma_1 = 1.602$, and $\gamma_2 = 1.288$)	$L_{1/2} = 0.061$; $L_{\text{h.r.}} = 0.114$ ($K = 2000$)
6.9	Moderately unstable detonation ($2\text{H}_2 + \text{O}_2 + 5.6\text{N}_2$, $\gamma_1 = 1.405$, and $\gamma_2 = 1.185$)	$L_{1/2} = 0.140$; $L_{\text{h.r.}} = 0.222$ ($K = 2000$)
12.7	Highly unstable detonation ($\text{C}_3\text{H}_8 + 5\text{O}_2 + 9\text{N}_2$, $\gamma_1 = 1.336$, and $\gamma_2 = 1.161$)	$L_{1/2} = 14.799$; $L_{\text{h.r.}} = 5.956$ ($K = 2000$)

2.4. Computational Cases

The detonation cell structure can be classified into the weakly, moderately, and highly unstable regimes [18], depending on the thermodynamic and chemical kinetic characteristics of the reactants. Representative cases for these regimes are selected based on the work of Austin et al. [18]. Table 3 lists the reduced activation energies (θ) and specific heat ratios of reactants and products. The former (also known as reduced activation temperature) is defined as the activation temperature normalized by the von Neumann value

$$\theta \equiv \frac{T_a}{T_{\text{VN}}} \equiv \frac{E_a}{R_1 T_{\text{VN}}}, \tag{13}$$

where E_a is the activation energy and T_{VN} is the temperature corresponding to the von Neumann peak. A higher activation energy results in more unstable (or irregular) detonation phenomena [5].

3. ZND STRUCTURE

The ZND structure of a detonation wave is first determined to provide a basis for the multidimensional detonation study. With the assumption of steady state and one-dimensionality, the conservation laws in Eq. (1) reduce to the following set of nonlinear algebraic equations:

$$\rho u = \rho_1 u_1, \tag{14}$$

$$\rho u^2 + p = \rho_1 u_1^2 + p_1, \tag{15}$$

$$\frac{\gamma}{\gamma - 1} \frac{p}{\rho} + \frac{1}{2} u^2 = \frac{\gamma_1}{\gamma_1 - 1} \frac{p_1}{\rho_1} + \frac{1}{2} u_1^2 + Zq, \tag{16}$$

$$\frac{\partial Z}{\partial x} = \frac{1}{u} (1 - Z) K \exp\left(-\frac{T_a}{T}\right). \tag{17}$$

The pressure p , density ρ , and velocity u can be derived as functions of the reaction progress variable Z as follows:

$$\frac{p}{p_1} = \frac{\gamma_1 M_1^2 + 1}{\gamma M^2 + 1}, \tag{18}$$

$$\frac{\rho}{\rho_1} = \frac{\gamma_1 M_1^2 (\gamma M^2 + 1)}{\gamma M^2 (\gamma_1 M_1^2 + 1)}, \tag{19}$$

$$\frac{u}{u_1} = \frac{\gamma M^2 (\gamma_1 M_1^2 + 1)}{\gamma_1 M_1^2 (\gamma M^2 + 1)}. \tag{20}$$

Here

$$M = \sqrt{\frac{[\gamma - (\gamma - 1)B] - \sqrt{\gamma^2 - (\gamma^2 - 1)B}}{\gamma(\gamma - 1)(B - 1)}}, \tag{21}$$

$$B = \frac{2\gamma_1^2 M_1^2 \left(1 + \frac{\gamma_1 - 1}{2} M_1^2 + Z\hat{q}\right)}{(\gamma_1 - 1)(\gamma_1 M_1^2 + 1)^2},$$

$$M_1 = \frac{u_1}{\sqrt{\gamma_1 p_1 / \rho_1}}, \quad \hat{q} = q \frac{(\gamma_1 - 1) \rho_1}{\gamma_1 p_1}. \tag{22}$$

The temperature T is then obtained through the equation of state, Eq. (4). Furthermore, if the Mach number M_1 of the incoming flow equals its CJ counterpart, i.e.,

$$M_1 = M_{D,\text{CJ}} \equiv \left[\left(\frac{\gamma_2^2 - 1}{\gamma_1 - 1} \hat{q} + \frac{\gamma_2^2 - \gamma_1}{\gamma_1^2 - \gamma_1} \right) + \sqrt{\left(\frac{\gamma_2^2 - 1}{\gamma_1 - 1} \hat{q} + \frac{\gamma_2^2 - \gamma_1}{\gamma_1^2 - \gamma_1} \right)^2 - \left(\frac{\gamma_2}{\gamma_1} \right)^2} \right]^{1/2}, \tag{23}$$

then Eqs. (18)–(21) will give the von Neumann and CJ states with Z set to 0 and 1, respectively.

By substituting the expressions of u and T in terms of Z into Eq. (17), an ordinary differential equation for the reaction progress variable is obtained as an initial-value problem in space. It is solved numerically by a four-stage Runge–Kutta method with the von Neumann state taken at $x = 0$. As the integration proceeds, a final condition corresponding to the CJ state is reached with $Z = 1$. As an illustration, Fig. 2 shows the calculated ZND detonation wave structure for the case of $\theta = 6.9$ and $K = 1000$.

To investigate the scaling issue discussed in Sec. 3, a series of one-dimensional calculations is performed for

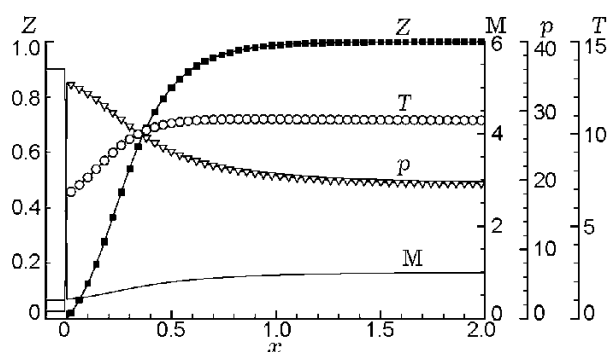


Fig. 2. Calculated ZND structure for the case of $\theta = 6.9$ and $K = 1000$ with a grid size $\Delta x = 0.01$.

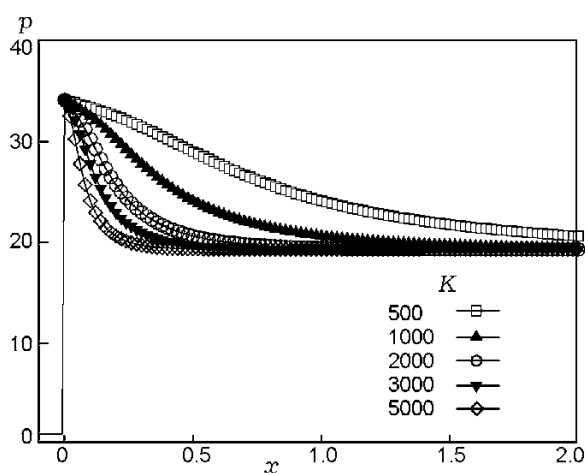


Fig. 3. Effect of the preexponential factor K on pressure distributions for ZND detonation waves ($\theta = 6.9$ and $\Delta x = 0.01$).

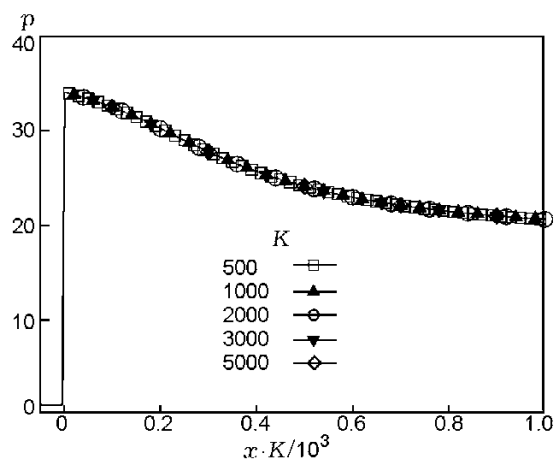


Fig. 4. Effect of the preexponential factor K on pressure distributions for ZND detonation waves in the scaled coordinate; $\theta = 6.9$ and $\Delta x = 0.01$.

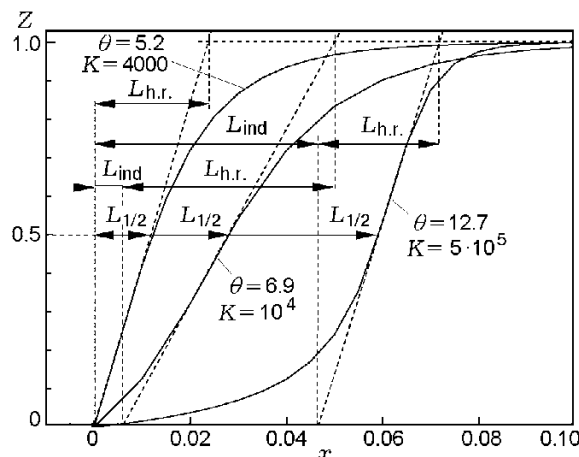


Fig. 5. Distribution of the reaction progress variable Z within the ZND wave structure and definitions of chemical distances.

the case of $\theta = 6.9$ with the preexponential factor K in the range of 500–5000. The length of the computational domain is fixed to 2.0, and the number of grid points is 201. Figure 3 shows the pressure distributions. For $K < 500$, the computational domain appears to be too small to cover the entire ZND structure; on the other hand, for $K > 5000$, the grid size becomes too coarse to resolve the structure, because of numerical stiffness. Figure 4 shows that all the pressure profiles collapse into one single curve in a coordinate scaled by the preexponential factor K , due to its linear proportionality to the length scale. The same phenomenon occurs if the grid size is varied and K remains fixed. The results presented in Fig. 4 clearly address the scaling issue discussed in Sec. 1.3.

The ZND structures for the three cases given in Table 3 are calculated. Figure 5 shows the distributions of the reaction progress variable. In general, the reaction zone is composed of chemical-induction and heat-release subregions, which can be conveniently and unambiguously divided by the intersection point of the x coordinate and the maximum-slope tangent line to the Z profile, as displayed in the figure. The induction zone starts from the origin to the intersection point on the x axis, and the heat-release zone extends from this point to another intersection point between the tangent line and the line $Z = 1$. The three different regimes of detonation can be characterized by the induction-zone (L_{ind}) and the heat-release zone ($L_{h.r.}$) lengths. Weakly unstable detonation has almost no induction zone due to the low activation energy and very high temperature at the von Neumann peak. For moderately unstable detonation, the induction zone is relatively shorter than the heat-release zone. For highly unstable detonation,

the induction zone is several times longer than the heat-release zone, due to the high activation energy.

The half-reaction zone, defined as the region from $Z = 0$ to $Z = 0.5$, is also depicted in Fig. 5. It covers the induction zone and part of the heat-release zone. The corresponding half-reaction zone length ($L_{1/2}$) has been widely used to characterize the grid resolutions in simulating detonation cell structures [5, 8, 9, 11, 13]. However, since the flow properties vary smoothly within the induction zone but rapidly within the heat-release zone, the grid resolution within the heat-release zone appears to play a more important role than that in the overall or half-reaction zones. The steep gradients of flow properties in the heat-release region often cause numerical stiffness problems in chemical-kinetics and numerical-flux calculations. Thus, the grid resolution within the heat-release zone of the ZND structure is selected as a primary parameter in the present work.

4. WEAKLY UNSTABLE DETONATION

The theoretical and numerical framework outlined in Sec. 1 has been used to study two-dimensional detonation phenomena in various regimes. Calculations were first carried out for weakly unstable detonation with a reduced activation temperature $\theta = 5.2$. The preexponential factor K varied in the range of 200–20,000. To initialize the formation of detonation cell structures, the one-dimensional analysis described in Sec. 3 was applied to provide the initial conditions for the flowfield, with the ZND structure inclined in the transverse direction. Figure 6 shows the distributions of the reaction progress variable Z for the ZND waves with $K = 500$ –5000 from one-dimensional calculations. The length of the computational domain is fixed to 2.0, and the grid size is $\Delta x = 0.01$. The combustion progresses rapidly behind the von Neumann peak, without a distinguishable chemical-induction zone. The reaction progress variable increases linearly behind the shock wave and smoothly transits to the equilibrium CJ condition. For $K < 500$, the computational domain is not sufficiently large to cover the entire reaction zone. On the other hand, for $K > 5000$, the grid size of $\Delta x = 0.01$ becomes too coarse to resolve the detonation wave structure.

4.1. Baseline Case with $K = 2000$

The baseline case with $K = 2000$ was first simulated and studied in detail. The grid contains 501×201 cells, and the length of the computational domain is

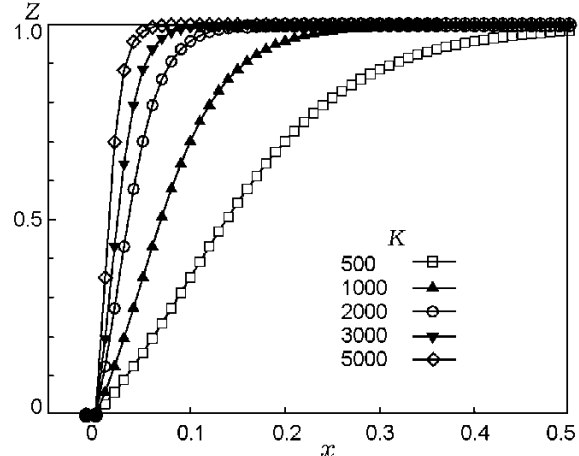


Fig. 6. Distribution of the reaction progress variable Z for the ZND wave for different preexponential factors (weakly unstable detonation; $\theta = 5.2$ and $\Delta x = 0.01$).

≈ 5.1 , as summarized in Table 2. The grid size is $\Delta x = 0.005$ in the upstream region $0 \leq x \leq 2$. The Courant–Friedrichs–Lewy (CFL) number is 0.5. The characteristic boundary conditions are applied at the exit boundary.

Figure 7 shows the temporal evolution of the temperature and pressure fields. Each snapshot covers a spatial region of 0.22×1 , and the time span between each pair of adjacent snapshots is 0.22. The detailed structure of the detonation wave front is well captured. The trajectories of triple points that form detonation cells are also observed. Figure 8 shows the corresponding numerical smoke-foil record, exhibiting quite regular cells. The entire channel width ($W = 1$) covers 1.5 cells. The cell width of 0.67 is about 28 times the half-reaction length ($L_{1/2} = 0.024$).

4.2. Preexponential Factor

The influence of the preexponential factor K is explored in the range of 200–20,000, with the grid 301×101 ($\Delta x = 0.01$). This study also provides direct information about the grid-resolution requirement, as discussed in Sec. 1.3 in connection with the scaling issue. The ZND structure for $K = 5000$ is used as an initial condition for the cases with K greater than 10,000, since the ZND structure for those cases could not be obtained using the grid spacing $\Delta x = 0.01$. For $K < 200$, the detonation wave cannot be fully settled down and is blown out of the computational domain.

Figure 9 shows the structures of the detonation wave fronts for $K = 500, 1000, 2000, 5000, 10,000,$ and $20,000$. Each frame covers a spatial region of 1×1 in

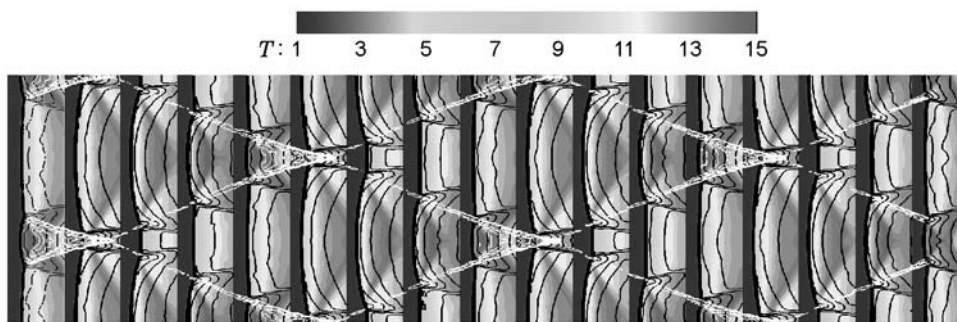


Fig. 7. Temperature and pressure fields (dark curve) and smoke-foil record (white curve), showing the temporal evolution of the detonation wave front for the baseline case ($\theta = 5.2$, $K = 2000$, and $\Delta x = 0.005$).

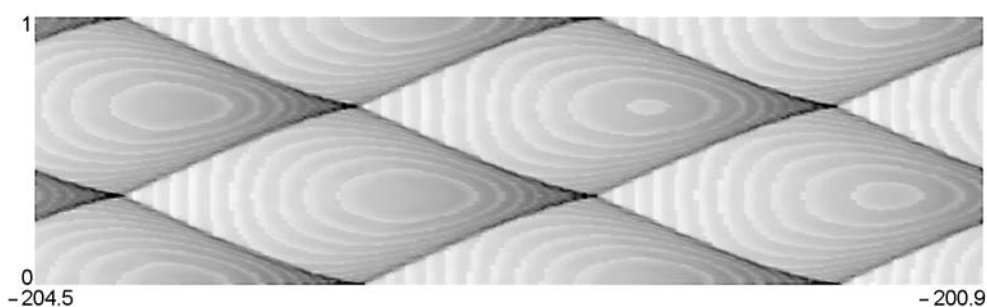


Fig. 8. Numerical smoke-foil record for weakly unstable detonation wave; baseline case ($\theta = 5.2$, $K = 2000$, and $\Delta x = 0.005$).

the axial and transverse directions, respectively. The pressure contours are overlaid with the distributions of the reaction progress variable. For $K = 500$ and 1000 , only one triple point, along with a very wide reaction zone, is observed, illustrating the typical triple-shock structure, which involves a Mach stem and an incident and a transverse shock [1]. The reaction zone is thicker behind the relatively weaker incident shock than behind the relatively stronger Mach stem. As the preexponential factor K increases, the fast reaction gives rise to a narrower combustion zone. For $K = 2000$ and 5000 , the number of triple points increases, and a weakly unstable detonation is observed with evenly spaced triple points. The wave front structure disappears, however, for $10,000$ and $20,000$, mainly due to the insufficient grid resolution for simulating the triple shock structure. Nonetheless, the calculation can still capture the wave front as a steady one-dimensional detonation wave.

Figure 10 shows the numerical smoke-foil records for $K = 200$ – $10,000$. Quite regular cellular structures are observed, except for $K = 10,000$, for which the present grid resolution of $\Delta x = 0.01$ appears to be insufficient. In general, the number of cells increases with the preexponential factor. For $K = 200$, 500 , and 1000 , the channel width only accommodates half a cell. The

number of cells increases to 1.5 and 4.5 for $K = 2000$ and 5000 , respectively. It can be expected that, as more cells fit across the channel width, the number of cells will become proportional to the preexponential factor K . This kind of relation between the number of cells and the preexponential factor is quite similar to that between the channel and cell widths studied by Nikolic et al. [9]. The results are also consistent with experimental observations that the detonation cell width tends to adjust its size to the channel width for narrow channels, but becomes irrelevant to the channel width in large channels [1].

The requirement for resolving detonation cells can be obtained by transferring the results to their dimensional counterpart. The dimensional grid size is related to the fixed nondimensional value ($\Delta x = 0.01$) as

$$\widetilde{\Delta x} \equiv \Delta x \cdot L^* \equiv \Delta x \cdot K u^* / \tilde{K}. \quad (24)$$

If the dimensional preexponential factor \tilde{K} and velocity scale u^* are fixed, then $\widetilde{\Delta x}$ is proportional to the preexponential factor K . The aforementioned observation that the detonation cells are resolved for $K \leq 5000$, thus, indicates that, for this type of specific problems with $\theta = 5.2$ and any given \tilde{K} and u^* , the dimensional grid size should be $\widetilde{\Delta x} \leq \Delta x \cdot K u^* / \tilde{K} = 50 u^* / \tilde{K}$.

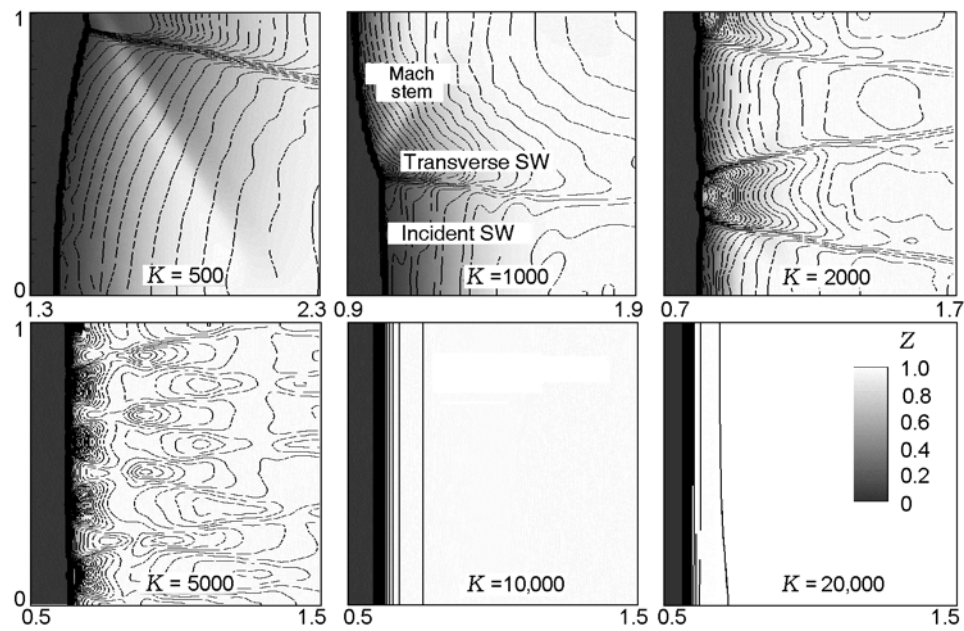


Fig. 9. Snapshots of pressure contours (line) and distributions of the reaction progress variable for different preexponential factors, illustrating the structure of weakly unstable detonation wave fronts (301×101 grid; $\Delta x = 0.01$).

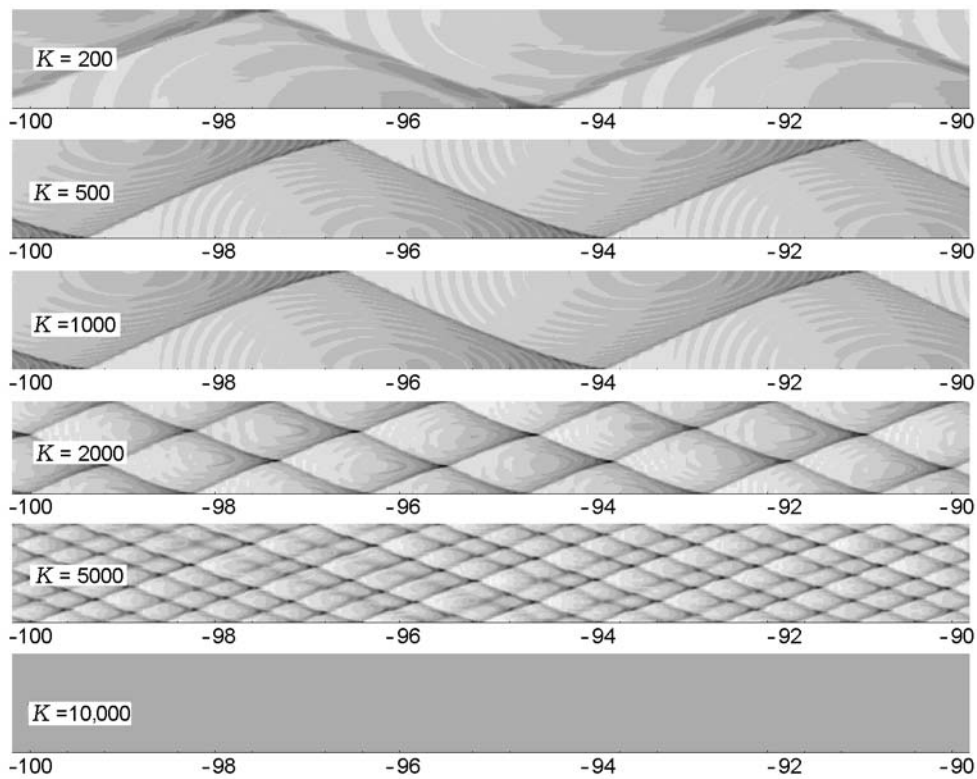


Fig. 10. Numerical smoke-foil records for a weakly unstable detonation wave (301×101 grid; $\Delta x = 0.01$).

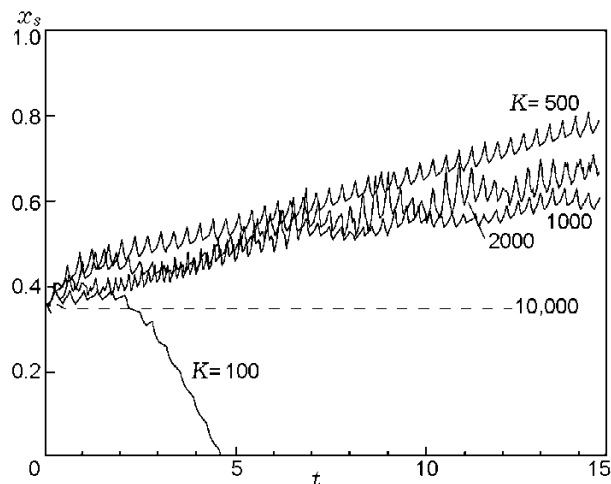


Fig. 11. Temporal evolution of the shock wave location along the centerline of the computational domain for weakly unstable detonation (301×101 grid; $\Delta x = 0.01$).

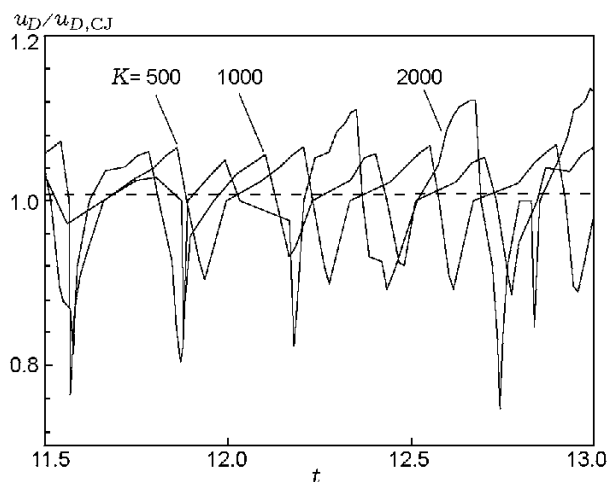


Fig. 12. Temporal variation of the detonation velocity (0301×101 grid; $\Delta x = 0.01$).

Figure 11 shows the temporal variation of the leading shock wave location along the centerline of the computational domain in the range of $K = 100$ – $10,000$. For $K = 100$, as pointed out earlier, the detonation wave fails to remain within the computational domain. For $K = 10,000$, the shock wave location is unchanged, representing a steady-state solution. For other cases, the shock wave oscillates regularly within the uniform grid region ($0 \leq x \leq 2$) and moves slowly downstream. The averaged shock velocity is slightly smaller than the CJ detonation velocity by 1–3%.

Figure 12 shows the temporal variation of the shock wave velocity. The ratio of the shock wave velocity to the CJ detonation velocity varies roughly from 0.8 to 1.1, falling in the range for ordinary detonations [1]. The shock wave velocity reaches its highest value just after the collision of two triple points, corresponding to an overdriven detonation. The wave then weakens gradually, and the velocity ratio becomes 1.0 at about the middle of the cell. The velocity ratio continuously decreases to its minimum value immediately before another collision of two triple points.

4.3. Computational Domain Length and Exit Boundary Conditions

Ideally, the computational domain should be long enough that the CJ state is reached within the domain. In practice, however, the domain length is limited to reduce the computational cost. Choosing an appropriate computational domain and exit boundary conditions, thus, becomes an important issue in simulations. If a very short domain is used, the unstable detonation wave may be blown out of the domain regardless of the grid resolution, because the CJ condition cannot be met at the exit boundary and an improper subsonic boundary breaks the force balance necessary for stabilizing the detonation wave within the computational domain.

A parametric study is carried out for the case of $\theta = 5.2$ and $K = 1000$, with the length of the computational domain (x_{exit}) ranging from 1.0 to 28.2. The grid size in the uniform region is fixed as 0.01, and the characteristic exit boundary condition is used. Figure 13 shows the temporal variation of the shock wave location along the centerline of the computational domain. The detonation wave is not stabilized within computational domains $x_{\text{exit}} < 1.5$, whereas the regularly oscillating detonation is attained for longer domains. The shock wave locations are almost identical for $x_{\text{exit}} \geq 2.0$, suggesting that the domain length has very little influence on the wave front structure once it exceeds a critical limit (e.g., 2.0 for the current case) such that the wave can be stabilized within the domain. Figure 14 shows the time history of the Mach number spatially averaged in the transverse direction at the exit boundary. As the computational domain gets longer, the variation in the exit Mach number becomes smaller and smoother. A nearly constant exit Mach number of $M_{\text{exit}} = 0.996$ is observed for a domain length of $x_{\text{exit}} = 28.2$.

The influence of the exit boundary condition is examined for two domain lengths, 1.5 and 5.2. Figure 15 shows the time history of the post-shock pressure with three different exit boundary conditions, as discussed

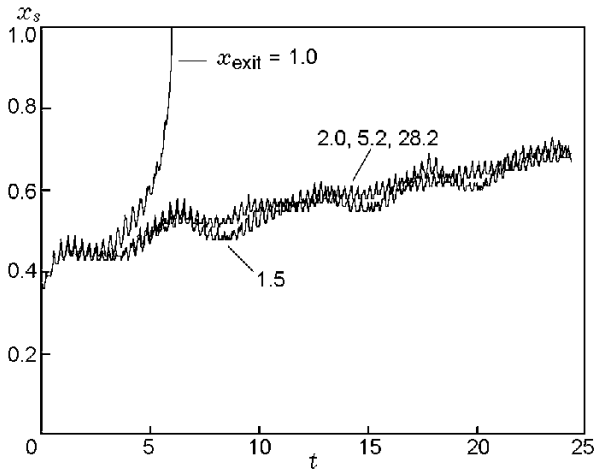


Fig. 13. Temporal evolution of the shock wave location along the centerline of the computational domain for weakly unstable detonation with different domain lengths ($K = 1000$).

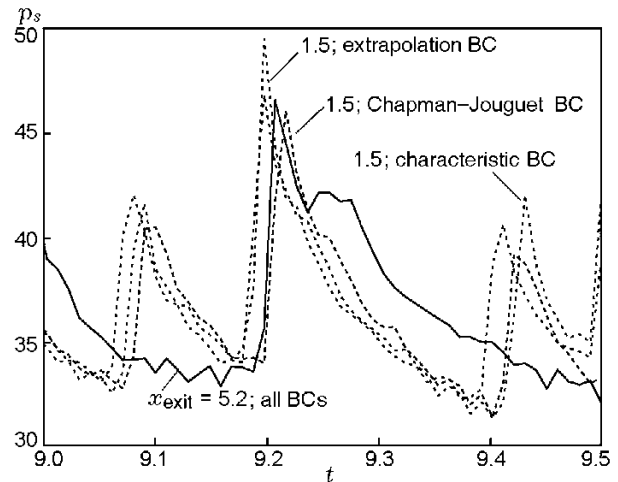


Fig. 15. Temporal evolution of the von Neumann peak pressure along the centerline of the computational domain for weakly unstable detonation with different exit boundary conditions ($K = 1000$).

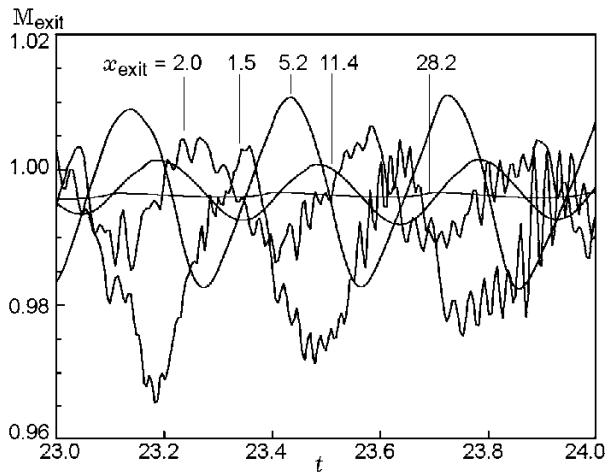


Fig. 14. Time history of the transversely averaged Mach number at the exit of the computational domain for weakly unstable detonation with different domain lengths ($K = 1000$).

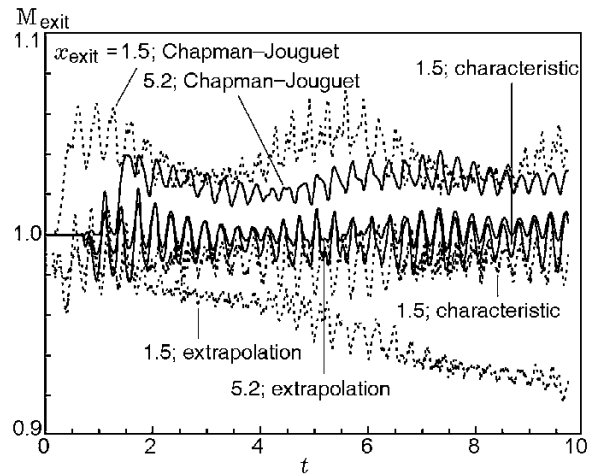


Fig. 16. Time history of the transversely averaged Mach number at the exit of the computational domain for weakly unstable detonation with various exit boundary conditions ($K = 1000$).

in Sec. 2.1. For a domain length $x_{\text{exit}} = 1.5$, the pressure history varies slightly for different boundary conditions. The results, however, are almost identical (up to six significant digits of the pressure data) for a domain length $x_{\text{exit}} = 5.2$. Thus, the exit boundary condition has a negligible effect on the wave front solution, if the computational domain is longer than a critical limit. Figure 16 shows the time history of the transversely averaged Mach number at the exit plane. The forced CJ boundary condition gives rise to an unphysical exit Mach numbers greater than 1.0. The simple extrapola-

tion gives reasonable results for the longer domain but leads to continuous decay of the exit Mach number for the shorter domain. The characteristic boundary condition produces a Mach number oscillating slightly around unity and is, thus, more desirable. The influence of the exit boundary condition, certainly, becomes negligible if a sufficiently long computational domain is used.

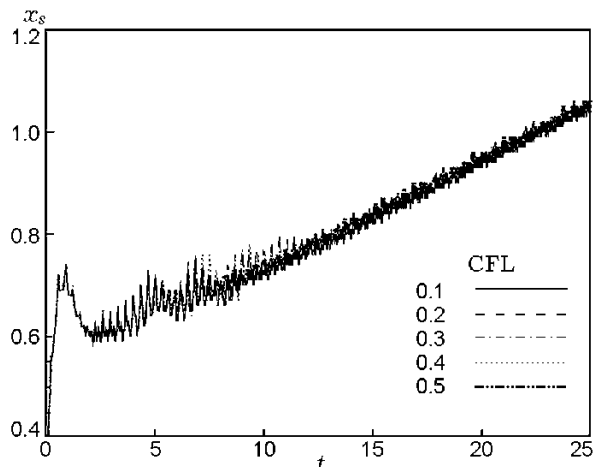


Fig. 17. Temporal evolution of the shock wave location along the centerline of the computational domain with different CFL numbers ($K = 2000$).

4.4. Time Step

For a given grid, the time step may affect the solution stability of the flow field and numerical diffusion. In the present work, the influence of the time step is examined by varying the CFL number from 0.1 to 0.5 for the case of $K = 2000$ with the 301×101 grid. Although the theoretical maximum limit of the current scheme permits a larger CFL number, a value of 0.5 is the practical maximum because of the stiffness associated with chemical source terms. On the other hand, for computational efficiency, a value of 0.1 is selected as the lower limit.

Figure 17 shows the temporal variation of the shock wave location. The results are very close for different CFL numbers. The shock wave moves slowly downstream at about the same speed and with the same oscillating frequency. The numerical smoke-foil records (not shown) are almost identical. Thus, both the cell structure and cell size are insensitive to the time step used.

4.5. Grid Resolution

A fine grid is always desirable for computation, but grid resolution is restricted practically by the strict limits on computational resources. In the present work, the issue of grid resolution has been partially addressed through the investigation of the effect of the preexponential factor K with a fixed grid. For completeness, this issue is further studied by changing the grid size employed in actual simulations. Three grids (301×101 ,

501×201 , and 901×401) with grid sizes of 0.01, 0.005, and 0.0025, as summarized in Table 2, are considered for the case of $K = 2000$. For reference, the half-reaction and heat-release zone lengths for such a case are 0.061 and 0.114, respectively.

Figure 18 shows the detonation wave front structures for different grids. As the grid becomes finer, the shock waves become thinner and the curvature of the leading shock increases. Other features vary little. Figure 19 shows the smoke-foil records. The number of cells across the channel width remains 1.5 for all three grids, demonstrating that a grid-independent cell size has been obtained.

5. MODERATELY UNSTABLE DETONATION

The moderately unstable detonation under consideration has a reduced activation temperature of $\theta = 6.9$. Figure 20 shows the distributions of the reaction progress variable Z for ZND waves with $K = 500$ – 5000 from one-dimensional calculations. The length of the computational domain is fixed to 2.0, and the grid size is $\Delta x = 0.01$. The combustion progresses rapidly behind the von Neumann peak with a narrow chemical-induction zone. If $K > 20,000$, the grid size of 0.01 becomes too coarse to resolve the detonation wave structure.

Figure 21 shows the structure of the detonation wave fronts for different preexponential factors from two-dimensional simulations with both 301×101 and 901×401 grids. In contrast to the weakly unstable cases, the wave front structure becomes more complex and irregular. The appearance of unreacted pockets, as indicated by the isolated dark regions behind the leading shock wave, is quite noticeable. A similar phenomenon was observed in experiments [18]. Differences in the wave front structure are observed between two grid resolutions. With the finer grid, more detailed structures, such as the dual triple points reported by Sharpe [11] and Hu et al. [12], are resolved.

Figure 22 shows the corresponding numerical smoke-foil records. Due to the increase in activation energy, the cell structure becomes more irregular than that of weakly unstable detonation. The cells are now nonuniform, with the ratio of the maximum and minimum cell sizes reaching about 2.0. In addition, with the finer grid, the secondary triple point, which is not resolved with the coarser grid, imprints an additional weaker track, as can be seen in the numerical smoke-foil records.

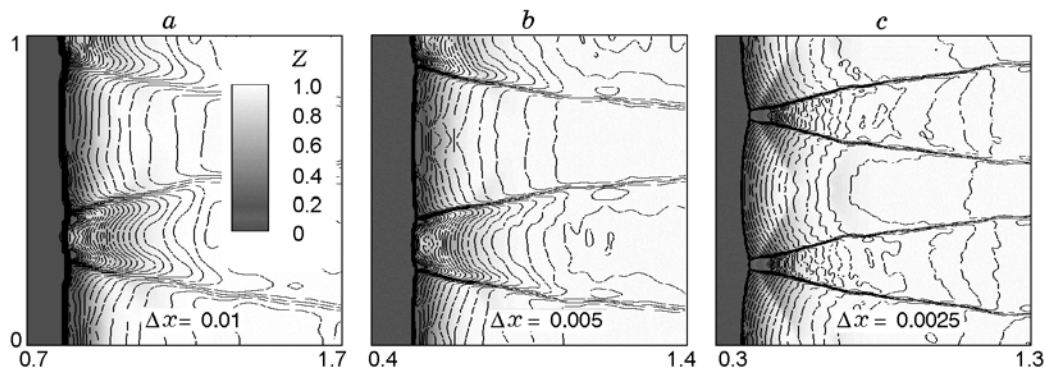


Fig. 18. Snapshots of pressure contours (curve) and distributions of the reaction progress variable Z illustrating the structures of weakly unstable detonation wave fronts from different grids: 301×101 (a), 501×201 (b), and 901×401 (c) ($\theta = 5.2$ and $K = 2000$).

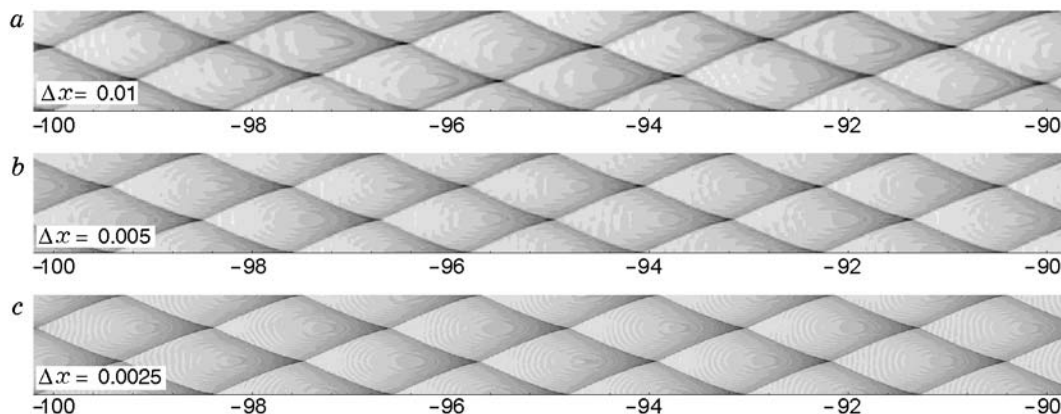


Fig. 19. Numerical smoke-foil records for a weakly unstable detonation wave from different grids: 301×101 (a), 501×201 (b), and 901×401 (c) ($\theta = 5.2$ and $K = 2000$).

6. HIGHLY UNSTABLE DETONATION

The highly unstable detonation under consideration has a reduced activation temperature of $\theta = 12.7$. Figure 23 shows the distributions of the reaction progress variable Z for ZND waves with $K = 10^5$ – 10^6 , from one-dimensional calculations with a grid size of $\Delta x = 0.01$. The induction zone is several times larger than the heat-release zone, so that a flat region exists behind the von Neumann peak, as displayed by the curve $Z(x)$ with $K = 10^5$.

Two-dimensional simulations were carried out with all three grids. It was found that, due to the strong irregularity of the highly unstable detonation, the cell structures could not be resolved with the 301×101 and 501×201 grids for a wide range of the preexponential factor K . Thus, only the results from the 901×401 grid are presented. Figure 24 shows the wave front structures for different preexponential factors. Compared

with the weakly and moderately unstable detonations, highly unstable detonations have much more irregular wave structures. The leading shock becomes severely wrinkled, as also reported in the experimental study of Austin et al. [18]. The high activation energy renders the reaction more sensitive to the flow temperature. Thus, the reaction zone lengths differ significantly behind the incident shock and the Mach stem, leading to a wide range of length scales within the front structure. Also to be observed are the multiple unreacted pockets behind the frontal reaction zone.

As a consequence of the highly unstable wave front structure, the numerical smoke-foil records shown in Fig. 25 display strongly irregular patterns. The maximum cell size is about 20 times larger than the minimum cell size, which is comparable to the experimentally reported maximum-to-minimum cell size ratios of 30 to 40 [18].

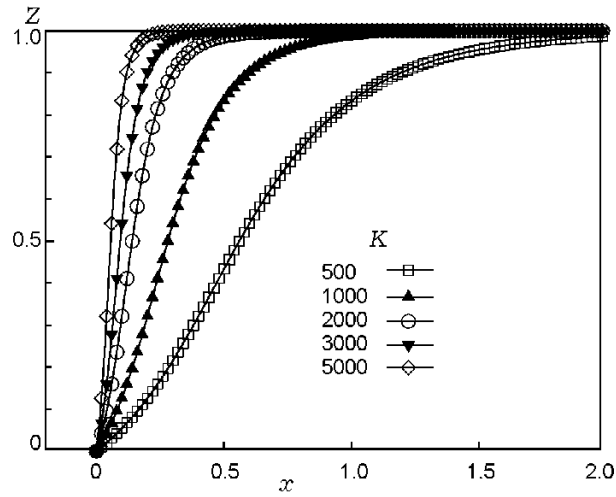


Fig. 20. Distribution of the reaction progress variable for the ZND wave at different preexponential factors (moderately unstable detonation; $\theta = 6.9$ and $\Delta x = 0.01$).

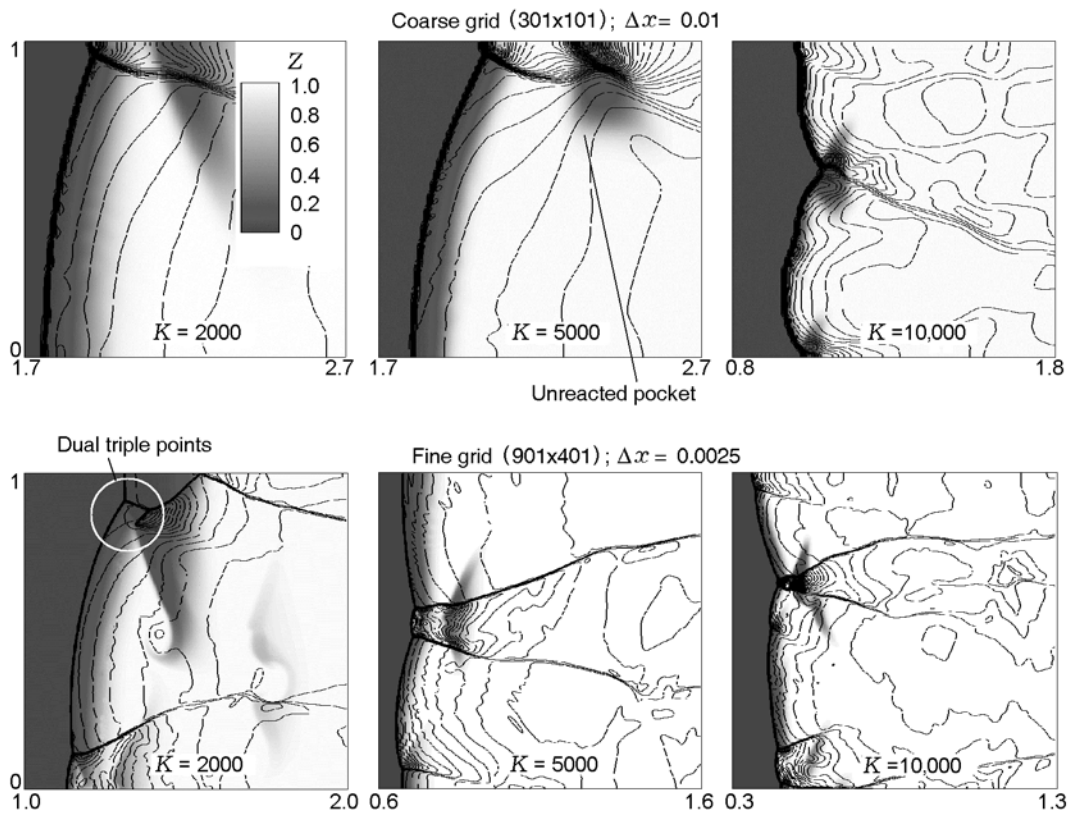


Fig. 21. Snapshots of pressure contours (curve) and distributions of the reaction progress variable Z , illustrating structures of moderately unstable detonation wave fronts from 301×101 and 901×401 grids.

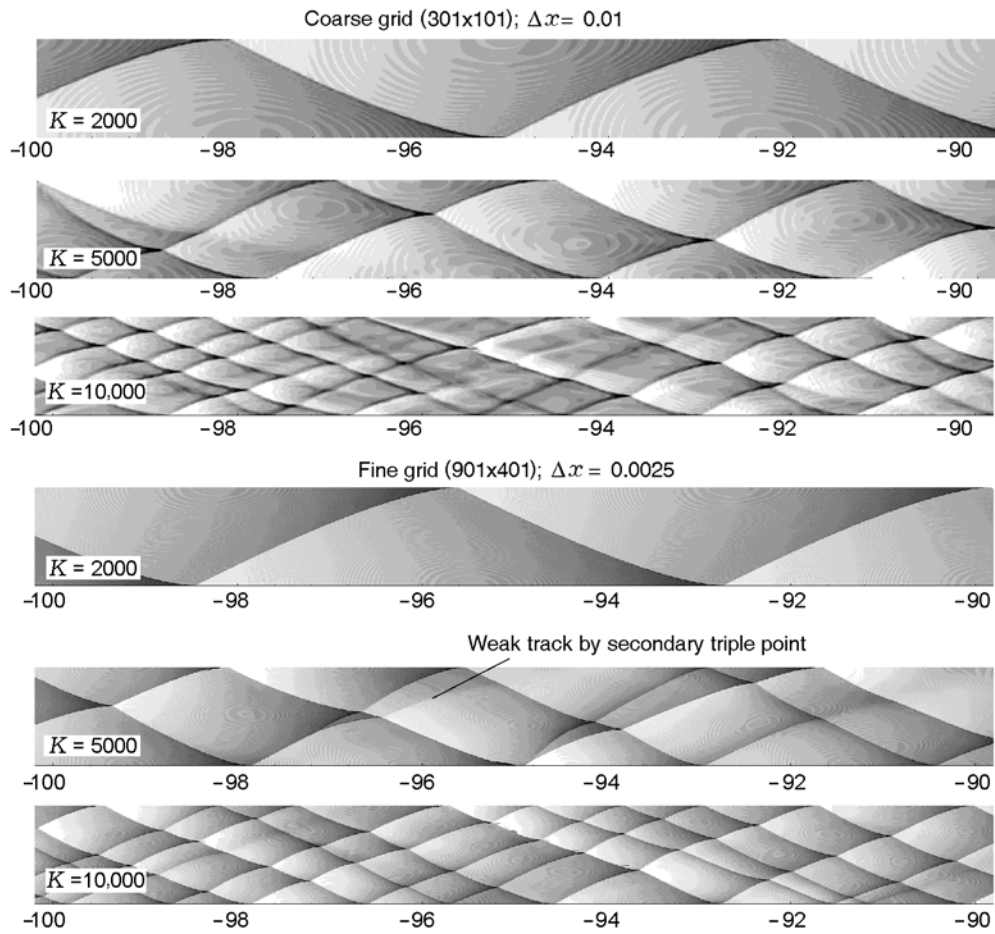


Fig. 22. Numerical smoke-foil records for moderately unstable detonation waves from 301×101 and 901×401 grids.

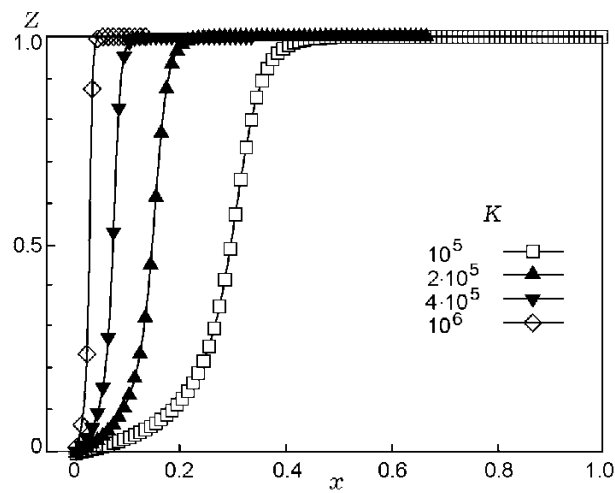


Fig. 23. Distribution of the reaction progress variable for ZND wave at different preexponential factors (highly unstable detonation; $\theta = 12.7$ and $\Delta x = 0.01$).

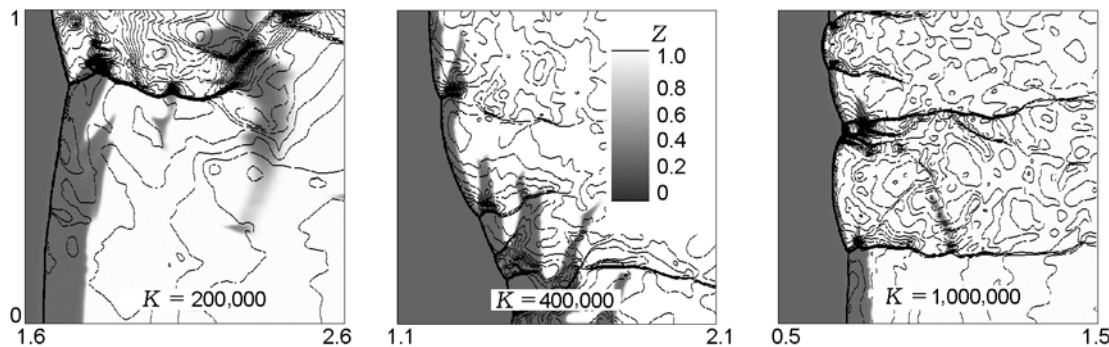


Fig. 24. Snapshots of pressure contours (curve) and distributions of the reaction progress variable Z illustrating structures of highly unstable detonation wave fronts (901×401 grid; $\Delta x = 0.0025$).

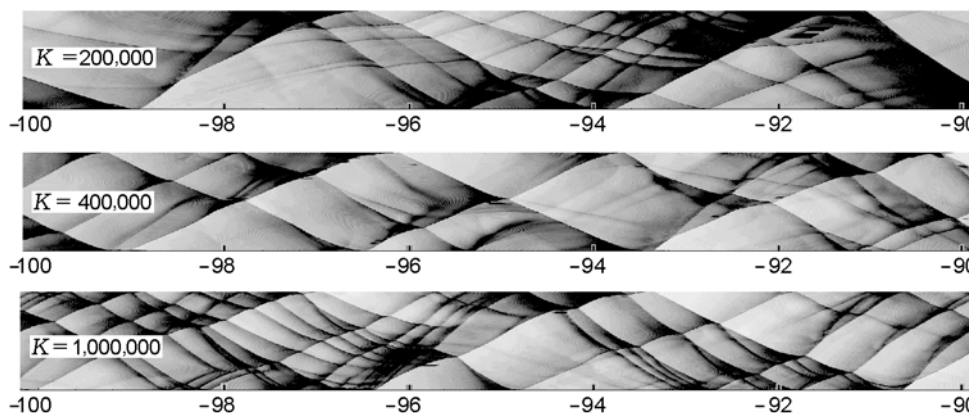


Fig. 25. Numerical smoked-foil records for a highly unstable detonation wave (901×401 grid; $\Delta x = 0.0025$).

7. GRID SIZE REQUIREMENT FOR CELL STRUCTURE SIMULATIONS

Table 4 summarizes the maximum possible preexponential factor K for each grid, such that the detonation cell structure could be resolved. In consideration of the scaling issues discussed in Sec. 1.3, the grid for such a value of K represents the coarsest grid able to resolve cell structures. Also included in the table is the number of grid points within the half-reaction and heat-release zones of the corresponding steady ZND structure. The number of grid points within the half-reaction zone is about 3 for weakly and moderately unstable detonations but increases to 12–15 for highly unstable detonations. On the other hand, the number of grid points within the heat-release zone is about 5, regardless of the degree of instability. It becomes clear that the number of grid points in the heat-release zone, rather than that in the half-reaction zone as widely used in previous studies, provides a more general guideline for the grid resolution requirement in simulating detonation cell struc-

tures. Based on the present results, we may formulate a general rule that the detonation cell structure can be properly resolved if a minimum of 5 grid points are included in the heat-release zone of the corresponding steady ZND detonation wave.

CONCLUSIONS

Several numerical issues on the simulation of cell structures were examined for weakly, moderately, and highly unstable detonations. The analysis was based on the two-dimensional conservation equations for an inviscid reacting flow with a one-step chemical kinetics model. The cellular patterns were obtained with numerical smoke-foil records, and the wave front structure and its evolution were explored in detail. The effects of the preexponential factor, grid size, time step, domain length, and exit boundary condition on the cellular structure and cell size were examined systematically. A general rule on the grid-size requirement for

TABLE 4

Maximum Possible Preexponential Factors K for Each Grid System That Produce Detonation Cell Structures and Number of Grid Points within Half-Reaction and Heat-Release Zones of a Steady ZND Structure

Grid system	Case	$L_{1/2}/\Delta x_{\min}$	$L_{h.r.}/\Delta x_{\min}$
Weakly unstable detonation ($\theta = 5.2$)			
301×101 ($\Delta x_{\min} = \Delta y = 0.01$)	$K = 5000$ ($L_{1/2} = 0.024$; $L_{h.r.} = 0.046$)	2.4	4.6
501×201 ($\Delta x_{\min} = \Delta y = 0.005$)	$K = 10,000$ ($L_{1/2} = 0.012$, $L_{h.r.} = 0.023$)	2.4	4.6
901×401 ($\Delta x_{\min} = \Delta y = 0.0025$)	$K = 20,000$ ($L_{1/2} = 0.006$, $L_{h.r.} = 0.012$)	2.5	4.8
Moderately unstable detonation ($\theta = 6.9$)			
301×101 ($\Delta x_{\min} = \Delta y = 0.01$)	$K = 10,000$ ($L_{1/2} = 0.028$, $L_{h.r.} = 0.044$)	2.8	4.5
501×201 ($\Delta x_{\min} = \Delta y = 0.005$)	$K = 20,000$ ($L_{1/2} = 0.014$, $L_{h.r.} = 0.022$)	2.8	4.5
901×401 ($\Delta x_{\min} = \Delta y = 0.0025$)	$K = 40,000$ ($L_{1/2} = 0.007$, $L_{h.r.} = 0.011$)	2.8	4.5
Highly unstable detonation ($\theta = 12.7$)			
301×101 ($\Delta x_{\min} = \Delta y = 0.01$)	Cell structure N/A		
501×201 ($\Delta x_{\min} = \Delta y = 0.005$)	$K = 400,000$ ($L_{1/2} = 0.074$, $L_{h.r.} = 0.030$)	14.8	6.0
901×401 ($\Delta x_{\min} = \Delta y = 0.0025$)	$K = 1,000,000$ ($L_{1/2} = 0.030$, $L_{h.r.} = 0.013$)	11.8	5.2

resolving detonation cell structures was proposed for the first time: a minimum of 5 grid points should be included in the heat-release zone of the corresponding steady ZND detonation wave. The present results indicate that the simulated cell sizes are not sensitive to either the time step or the grid size. The domain length and exit boundary condition are also of negligible influence, so long as the detonation wave can be stabilized within the domain.

This work was supported by the Office of Naval Research under Grant No. N00014-05-1-0159. The first author was also supported by the Korea Research Foundation (funded by the Korean Government MOEHRD) under Grant No. KRF-2006-521-D00061.

REFERENCES

1. W. Fickett and W. C. Davis, *Detonation Theory and Experiment*, Dover, New York (2000).
2. E. S. Oran, J. P. Boris, T. Young, et al., "Numerical simulations of detonations in hydrogen-air and methane-air mixtures," in: *Eighteenth Int. Symp. on Combustion* (1981), pp. 1641-1649.
3. S. Taki and T. Fujiwara, "Numerical simulation of triple shock behavior of gaseous detonation," *ibid.*, pp. 1671-1681.
4. K. Kailasanath, E. S. Oran, J. P. Boris, and T. R. Young, "Determination of detonation cell-size and the role of transverse-waves in two-dimensional detonations," *Combust. Flame*, **61**, No. 3, 199-209 (1985).
5. A. Bourlioux and A. J. Majda, "Theoretical and numerical structure for unstable two-dimensional detonations," *Combust. Flame*, **90**, Nos. 3-4, 211-229 (1992).
6. E. S. Oran, J. W. Weber, E. I. Stefaniw, et al., "A numerical study of a two-dimensional H_2 - O_2 -Ar detonation using a detailed chemical reaction model," *Combust. Flame*, **113**, Nos. 1-2, 147-163 (1998).
7. V. N. Gamezo and D. Desbordes, "Formation and evolution of two-dimensional cellular detonations," *Combust. Flame*, **116**, Nos. 1-2, 154-165 (1999).
8. S. Singh, J. M. Powers, and S. Paolucci, "Detonation solutions from reactive navier-stokes equations," AIAA Paper No. 1999-0966 (1999).
9. M. Nikolic, D. N. Williams, and L. Bauwens, "Detonation cell sizes — A numerical study," AIAA Paper No. 1999-0967 (1999).
10. A. I. Gavrikov, A. A. Efimenko, and S. B. Dorofeev, "A model for detonation cell size prediction from chemical kinetics," *Combust. Flame*, **120**, Nos. 1-2, 19-33 (2000).

11. G. J. Sharpe, "Transverse waves in numerical simulations of cellular detonations," *J. Fluid Mech.*, **447**, 31–51 (2001).
12. X. Y. Hu, B. C. Khoo, D. L. Zhang, and Z. L. Jiang, "The cellular structure of a two-dimensional $H_2/O_2/Ar$ detonation wave," *Combust. Theory Model.*, **8**, No. 2, 339–359 (2004).
13. Z. Liang and L. Bauwens, "Cell structure and stability of detonations with a pressure-dependent chain-branching reaction rate model," *Combust. Theory Model.*, **9**, No. 1, 93–112 (2005).
14. F. Pintgen, C. A. Eckett, J. M. Austin, and J. E. Shepherd, "Direct observations of reaction zone structure in propagating detonations," *Combust. Flame*, **133**, No. 3, 221–229 (2003).
15. J. Y. Choi, D. W. Kim, I. S. Jeung, F. H. Ma, and V. Yang, "Cell-like structure of unstable oblique detonation wave from high-resolution numerical simulation," in: *Proc. of the Combust. Inst.*, **31**, No. 2, 2473–2480 (2007).
16. J. Y. Choi, I. S. Jeung, and Y. Yoon, "Computational fluid dynamics algorithms for unsteady shock-induced combustion. Part 1: Validation," *AIAA J.*, **38**, No. 7, 1179–1187 (2000).
17. J. Y. Choi, I. S. Jeung, and Y. Yoon, "Computational fluid dynamics algorithms for unsteady shock-induced combustion. Part 2: Comparison," *ibid.*, pp. 1188–1195.
18. J. M. Austin, F. Pintgen, and J. E. Shepherd, "Reaction zones in highly unstable detonations," in: *Proc. of the Combust. Inst.*, **30**, No. 2, 1849–1858 (2005).